

Numerical study of effects of light polarization, scatterer sizes and orientations on near-field coherent anti-Stokes Raman scattering microscopy

Jian Lin¹, Haifeng Wang², Wei Zheng¹, Fake Lu¹, Colin Sheppard¹, and Zhiwei Huang^{1*}

¹Bioimaging Laboratory, Department of Bioengineering, Faculty of Engineering,
National University of Singapore, Singapore 117576

²Data Storage Institute, A*STAR, Singapore

*Corresponding author: biehzw@nus.edu.sg

Abstract: We employ the finite-difference time-domain (FDTD) technique as a numerical approach to studying the effects of polarization, scatterers' sizes and orientations on near-field coherent anti-Stokes Raman scattering (CARS) microscopy imaging. The results show that to acquire better image contrast and larger near-field CARS signals, the scatterers with diameters of less than three-eighths of the pump field wavelength (λ_p) are preferable to be oriented along the polarization direction of the excitation light fields. It is also found that when the scatterers' sizes are smaller than half a wavelength of the pump field, the perpendicular polarization component of the induced near-field CARS radiations is strictly confined within the regions at the scatterer-water interface or the subsurface of scatterers, yielding a high image contrast (up to 200) with a spatial resolution of $\lambda_p/16$. This study indicates that perpendicular polarization components of near-field CARS microscopy could be used to uncover very fine structures of intra- and/or inter-cellular organelles in cells with nanoscale resolutions.

©2009 Optical Society of America

OCIS codes: (180.6900) Three-dimensional microscopy; (190.4380) Nonlinear optics, four-wavemixing; (300.6230) Spectroscopy, coherent anti-Stokes Raman scattering

References and links

1. C. L. Evans, E. O. Potma, M. Puoris'haag, D. Côté, C. P. Lin, and X. S. Xie, "Chemical imaging of tissue in vivo with video-rate coherent anti-Stokes Raman scattering microscopy," *Proc. Natl. Acad. Sci.* **102**, 16807-16812 (2005).
2. A. Zumbushch, G. R. Holtom, and X. S. Xie, "Three-dimensional vibrational imaging by coherent anti-Stokes Raman scattering," *Phys. Rev. Lett.* **82**, 4142-4145 (1999).
3. C. L. Evans, X. Xu, S. Kesari, X. S. Xie, S. T. C. Wong, and G. S. Young, "Chemically-selective imaging of brain structures with CARS microscopy," *Opt. Express* **15**, 12076-12087 (2007).
4. E. Potma, W. P. de Boeij, P. J. van Haastert, and D. A. Wiersma, "Real-time visualization of intracellular hydrodynamics in single living cells," *Proc. Natl. Acad. Sci.* **98**, 1577-1582 (2001).
5. F. Lu, W. Zheng, and Z. Huang, "Heterodyne polarization coherent anti-Stokes Raman scattering microscopy," *Appl. Phys. Lett.* **92**, 123901 (2008).
6. J. X. Cheng and X. S. Xie, "Coherent anti-Stokes Raman scattering microscopy: instrumentation, theory, and applications," *J. Phys. Chem. B* **108**, 827-840 (2004).
7. X. Nan, E. O. Potma, and X. S. Xie, "Nonperturbative chemical imaging of organelle transport in living cells with coherent anti-Stokes Raman scattering microscopy," *Biophys. J.* **91**, 728-735 (2006).
8. F. Lu, W. Zheng, C. Sheppard, and Z. Huang, "Interferometric polarization coherent anti-Stokes Raman scattering (IP-CARS) microscopy," *Opt. Lett.* **33**, 602-604 (2008).
9. J. X. Cheng, S. Pautot, D. A. Weitz, and X. S. Xie, "Ordering of water molecules between phospholipid bilayers visualized by coherent anti-Stokes Raman scattering microscopy," *Proc. Natl. Acad. Sci.* **100**, 9826-9830 (2003).
10. G. W. Wurpel, H. A. Rinia, and M. Muller, "Imaging orientational order and lipid density in multilamellar vesicles with multiplex CARS microscopy," *J. Microsc.* **218**, 37-45 (2005).

11. H. Wang, Y. Fu, P. Zickmund, R. Shi, and J. X. Cheng, "Coherent anti-Stokes Raman scattering imaging of axonal myelin in live spinal tissues," *Biophys. J* **89**, 581-591 (2005).
12. X. S. Xie, J. Yu, and W. Yang, "Living cells as test tubes," *Science* **312**, 228-230 (2006).
13. F. Lu, W. Zheng and Z. Huang, "Elliptically polarized coherent anti-Stokes Raman scattering microscopy," *Opt. Lett.* **33**, 2842-2844 (2008).
14. T. T. Le, I. M. Langohr, M. J. Locker, M. Sturek, and J. X. Cheng, "Label-free molecular imaging of atherosclerotic lesions using multimodal nonlinear optical microscopy," *J. Biomed. Opt.* **12**, 054007 (2007).
15. F. Lu, W. Zheng, and Z. Huang, "Phase-controlled polarization coherent anti-Stokes Raman scattering microscopy," *J. Opt. Soc. Am. B* **25**, 1907-1913 (2008).
16. J. X. Cheng and X. S. Xie, "Green's function formulation for third-harmonic generation microscopy," *J. Opt. Soc. Am. B* **19**, 1604-1610 (2002).
17. T. Ichimura, N. Hayazawa, M. Hashimoto, Y. Inouye, and S. Kawata, "Tip-enhanced coherent anti-Stokes Raman scattering for vibrational nano-imaging," *Phys. Rev. Lett.* **92**, 220801 (2004).
18. Y. Saito, M. Motohashi, N. Hayazawa, M. Iyoki, and S. Kawata, "Nanoscale characterization of strained silicon by tip-enhanced Raman spectroscopy in reflection mode," *Appl. Phys. Lett.* **88**, 143109 (2006).
19. S. Kawata, I. Yasushi, and I. Taro, "Near-field optics and spectroscopy for molecular nano-imaging," *Sci. Progress* **87**, 25-49 (2004).
20. B. Jia, X. Gan, and M. Gu, "Direct observation of a pure focused evanescent field of a high numerical aperture objective lens by scanning near-field optical microscopy," *Appl. Phys. Lett.* **86**, 131110 (2005).
21. D. Courjon and C. Bainier, "Near field microscopy and near field optics," *Rep. Prog. Phys.* **57**, 989-1028 (1994).
22. B. Jia, X. Gan, and M. Gu, "Direct measurement of a radially polarized focused evanescent field facilitated by a single LCD," *Opt. Express* **13**, 6821-6827 (2005).
23. R. D. Schaller, J. Ziegelbauer, L. F. Lee, L. H. Haber, and R. J. Saykally, "Chemically selective imaging of subcellular structure in human hepatocytes with coherent anti-stokes Raman scattering (CARS) near-field scanning optical microscopy (NSOM)," *J. Phys. Chem. B* **106**, 8489-8492 (2002).
24. N. Djaker, D. Gachet, N. Sandeau, P. F. Lenne, and R. Hervé, "Refractive effects in coherent anti-Stokes Raman scattering microscopy," *Appl. Opt.* **45**, 7005-7011 (2006).
25. V. V. Krishnamachari and E. O. Potma, "Focus-engineered coherent anti-Stokes Raman scattering microscopy: a numerical investigation," *J. Opt. Soc. Am. A* **24**, 1138-1147 (2007).
26. C. Liu, Z. Huang, F. Lu, W. Zheng, D. W. Huttmacher, and C. Sheppard, "Near-field effects on coherent anti-Stokes Raman scattering microscopy imaging," *Opt. Express* **15**, 4118-4131 (2007).
27. K. S. Yee, "Numerical solution of initial boundary value problem involving Maxwell equations in isotropic media," *IEEE Trans. Antennas Propag.* **14**, 302-307 (1966).
28. A. Taflové, *Computational Electrodynamics: The Finite-Difference Time-Domain Method* (Artech House, Boston, 1995).
29. R. L. Sutherland, *Handbook of Nonlinear Optics* (Marcel Dekker, New York, 2003).
30. A. Volkmer, "Vibrational imaging and microspectroscopies based on coherent anti-Stokes Raman scattering microscopy," *J. Phys. D: Appl. Phys.* **38**, 59-81 (2005).
31. K. Takeda, Y. Ito, and C. Munakata, "Simultaneous measurement of size and refractive index of a fine particle in flowing liquid," *Meas. Sci. Technol.* **3**, 27-32 (1992).
32. M. Born and E. Wolf, *Principles of Optics* (7th edition, Cambridge University Press, Cambridge, 1999).

1. Introduction

Coherent anti-Stokes Raman scattering (CARS) microscopy is a nonlinear Raman imaging technique that has received great attention for biological and biomedical imaging due to its ability of real-time, nonperturbative chemical mapping of live unstained cells and tissue based on molecular vibrations [1-8]. For instance, CARS microscopy has been used to selectively identify cellular structures in live cells and tissue using the contrast provided by the spectral properties of lipids, proteins, nucleic acids, and water [4-8], as these molecular constituents are highly abundant in tissue and cells. The quantitative capabilities of CARS microscopy has also been utilized in determining local lipid density relative to the number of phospholipid bilayers, the ordering of water molecules in lipids, and the live cell hydrodynamics [9-11]. Recent advances in CARS microscopy illustrate that this label-free molecular imaging technique can also be combined with other nonlinear optical modalities (e.g., second-harmonic generation (SHG), third-harmonic generation (THG), two-photon excitation fluorescence (TPEF), etc.) for better characterization of various biochemicals and biomolecular structures and compositions in biomedical systems [12-15]. These results

demonstrate the usefulness of CARS microscopy as a compelling tool for probing biomolecules in live tissue and cells selectively, noninvasively, and quantitatively.

It is known that the CARS signal generated from a given sample is proportional to the product of the density of molecules, the square of the pump field intensity, and the Stokes field intensity. As such, under a spatially uniform illumination condition, the CARS technique can be used to determine the density of the molecules and the molecular structures in samples. This is the fundamental assumption in most wide-field or far-field studies on CARS microscopy [16]. However, the resonant Raman signal, in fact, is generated only from specific chemical bonds of molecules in the samples, and the CARS signal is determined by the local excitation light fields surrounding the chemical bonds, rather than just simply being determined by the illumination light fields. In the cases of CARS studies on small structures in cells or intracellular organelles, if the physical size of targets of interest (e.g., mitochondria, membranes) is equivalent to or even smaller than the wavelength of excitation light used, it is expected that the evanescent waves generated due to the near-field effects could dominate the local light fields within the molecule, and vary with a number of near-field factors such as the refractive index mismatch, edge effect, surface roughness, etc [17, 18]. That is, the spatially uniform illumination light field may not be the only excitation light source for generating the CARS signals [19]. For a given molecule, the induced nonlinear polarization component depends not only on the nonlinear coefficient and the illumination light fields, but also on the local light field distribution [17, 20-22]. Hence, the near-field effects should be taken into account in CARS microscopy particularly on nano-molecular imaging [23].

A number of simulation methods based on geometric optics and wave optics, as well as the vectorial theory have been developed for studying the effects of various factors (e.g., refractive index mismatch, focal-field distributions) on CARS imaging [24-26]. Most of work focused on the situations in which there is only one spherical particle inside the focal volume of excitation light fields for CARS generations [26]. This assumption is different from the practical situations whereby the biological cells or molecules are likely to aggregate each other in aqueous environments. If the sizes of these molecules or cells are equivalent to or smaller than the wavelength of excitation light, two or more of these scatterers could be excited simultaneously within the focal volume for CARS generations. Hence, in this work, we select two adjacent spherical nanoparticles as scatterers positioned inside the excitation focal volume to mimic the biological system for near-field CARS imaging. We also employ an advanced numerical technique- the finite-difference time-domain (FDTD) method [26-28] for investigating the influences of the excitation light polarization, the nanoparticles' sizes and orientations on the induced near-field CARS radiations.

2. Methods

2.1. Finite-difference time-domain (FDTD) method for simulations

In most practical cases, it is not possible to get the explicit solutions of Maxwell's equations due to complex boundary conditions; however, the numerical solutions can be calculated by using the finite-difference time-domain (FDTD) method, which was firstly reported by Yee [27]. In this method, the space is discretized into uniform or un-uniform grids with intervals to be equal or less than 1/10 time of the wavelength of the electromagnetic field employed, assuming that the refractive index and the electromagnetic field within each small grid are uniform, and the time is also divided into very small steps. Then the spatial and temporal differentials in Maxwell's equations can be approximated with finite differences, and thus the electric field at a given time and position $\mathbf{E}(\mathbf{r}, t_n)$ can be determined using the electric field of the position at previous time $\mathbf{E}(\mathbf{r}, t_{n-2})$ and the spatial finite-difference of the magnetic fields of surrounding grids at time t_{n-1} , where n is the index of time steps. The magnetic field $\mathbf{H}(\mathbf{r}, t_{n-2})$ can be obtained using the $\mathbf{H}(\mathbf{r}, t_{n-1})$ and the finite-difference of the electric field of surrounding grids at time t_n . After sufficient iterations on electric and magnetic fields, the

calculated electromagnetic field will converge to an explicit value anticipated by Maxwell's equations. If there is no free electric charge and current source in the medium of interest, Maxwell's equations can be written as

$$\begin{cases} \nabla \times \mathbf{H} = \frac{\partial \mathbf{D}}{\partial t} \\ \nabla \times \mathbf{E} = \frac{\partial \mathbf{B}}{\partial t} \end{cases} \quad (1)$$

where \mathbf{H} , \mathbf{D} , \mathbf{E} , and \mathbf{B} stand for magnetic field, electric displacement, electric field, and magnetic flux density, respectively. The discretized equations with standard uniform grids in temporal and spatial domains for electric fields in the FDTD simulator for 3-D coordinates are as follows [26]:

$$\begin{cases} E_x^{n+1}(i+0.5, j, k) = CA(\mathbf{r}) \cdot E_x^n(i+0.5, j, k) + CB(\mathbf{r})[(H_z^{n+0.5}(i+0.5, j+0.5, k) - H_z^{n+0.5}(i+0.5, j-0.5, k)) / \Delta y \\ \quad - (H_y^{n+0.5}(i+0.5, j, k+0.5) - H_y^{n+0.5}(i+0.5, j, k-0.5)) / \Delta z \\ E_y^{n+1}(i, j+0.5, k) = CA(\mathbf{r}) \cdot E_y^n(i, j+0.5, k) + CB(\mathbf{r})[(H_x^{n+0.5}(i, j+0.5, k+0.5) - H_x^{n+0.5}(i, j+0.5, k-0.5)) / \Delta z \\ \quad - (H_y^{n+0.5}(i+0.5, j+0.5, k) - H_y^{n+0.5}(i-0.5, j+0.5, k)) / \Delta x \\ E_z^{n+1}(i, j, k+0.5) = CA(\mathbf{r}) \cdot E_z^n(i, j, k+0.5) + CB(\mathbf{r})[(H_y^{n+0.5}(i+0.5, j, k+0.5) - H_y^{n+0.5}(i-0.5, j, k+0.5)) / \Delta x \\ \quad - (H_x^{n+0.5}(i, j+0.5, k+0.5) - H_x^{n+0.5}(i, j-0.5, k+0.5)) / \Delta y \end{cases} \quad (2)$$

where $CA(\mathbf{r}) = [2\varepsilon(\mathbf{r}) - \sigma(\mathbf{r})\Delta t] / [2\varepsilon(\mathbf{r}) + \sigma(\mathbf{r})\Delta t]$, $CB(\mathbf{r}) = 2\Delta t / [2\varepsilon(\mathbf{r}) + \sigma(\mathbf{r})\Delta t]$, and \mathbf{r} represent the position in the discretized grids. The discretized equations for the magnetic fields in the FDTD simulator can also be written similarly to the Eq. (2). After sufficient times of leapfrog iterations using these discretized equations, the electromagnetic field will converge to a stable value determined by the related boundary conditions. Based on this leapfrog approach in time-domain, FDTD simulator will determine not only the steady-state parameters (e.g., intensity distribution of the excitation light fields, phase and polarization of the localized light fields), but also the temporal evolution of these parameters against time.

2.2. Calculation of the induced third-order nonlinear polarization for CARS

The i -th component ($i = x, y, z$) of the induced third-order nonlinear polarization at the anti-Stokes frequency of $\omega_{as} = 2\omega_p - \omega_s$ can be expressed as

$$P_i^{(3)}(\mathbf{r}, \omega_{as}) = 3 \sum_{jkl} \chi_{ijkl}^{(3)} E_j(\mathbf{r}, \omega_p) E_k(\mathbf{r}, \omega_p) E_l^*(\mathbf{r}, \omega_s) \quad (3)$$

where $E_j(\mathbf{r}, \omega_p)$, $E_k(\mathbf{r}, \omega_p)$ and $E_l^*(\mathbf{r}, \omega_s)$ are the amplitudes of the pump and the Stokes beams in j , k , and l directions, respectively, and j , k , and l run over x , y , z ; $\chi_{ijkl}^{(3)}$ is the third-order nonlinear susceptibility of the medium. In FDTD simulations, we assume that scatterers are surrounded by water with a nonresonant contribution χ_{water}^{NR} ; while the scatterers comprise both resonant and nonresonant components, i.e., $\chi_{sca}^{(3)} = \chi_{sca}^{(3)R} + \chi_{sca}^{(3)NR}$, and $\chi_{sca}^{(3)NR} = \chi_{sca}^{(3)R}$ [25]. The nonresonant components of the nonlinear coefficients for both the water and scatterers are estimated using the equation $\chi_{xxyy}^{(3)NR} = \chi_{xyxy}^{(3)NR} = \chi_{yyxx}^{(3)NR} = \chi_{xxxx}^{(3)NR} / 3$ presumed that $\chi_{water}^{(3)NR} = \chi_{sca}^{(3)NR}$ [26]. If the scatterer has an isotropic vibrational symmetry, the

independent components in $\chi_{scd}^{(3)}$ are $\chi_{yyyx}^{(3)}$ and $\chi_{xyxy}^{(3)}$ [29], and the depolarization ratio-
 $\chi_{yyyx}^{(3)R} / \chi_{xxxx}^{(3)R}$ is 0 for an isotropic vibrational mode [30]. With all the $\chi_{ijkl}^{(3)}$ components being
known, the induced third-order polarization of the CARS signal can be numerically calculated
using Eq. (3).

2.3. Parameters of FDTD used for CARS simulations

In our simulations, the collinear pump and Stokes light beams are in parallel polarizations
with each other, and then collinearly focused onto the sample by passing through a high
numerical aperture (N.A. = 0.9) microscope objective as shown in Fig. 1(a). The calculation
volume was divided into cubic cells of $\lambda_p/60$ at each step, whereby λ_p (750 nm) is the
wavelength of the pump beam and the wavelength of Stokes beam λ_s is chosen to be 852 nm,
and then the generated CARS signal is at 670 nm, representing a resonant Raman shift of
 1600 cm^{-1} of mono-substituted benzene rings stretching vibrations in polystyrene beads [30].
The refractive indices of the scatterers (polystyrene beads) and surrounding medium (water)
are assumed to be 1.59 and 1.33, respectively [31]. To study the size effect on near-field
CARS signal generation, the scatterers' sizes are selected in the range of $\lambda_p/4$ to λ_p .

To investigate the influences of scatterers or nanoparticles' orientations with respect to
the excitation polarizations on near-field CARS radiations, three different configurations are
chosen as illustrated in Figs. 1(b, c, d), respectively. That is: (i) two nanoparticles are aligned
along the z direction while the polarizations of pump and Stokes light fields are in the y
direction; (b) two nanoparticles are arranged along the y direction with respect to the
polarization directions of pump and Stokes light fields being along the y direction; and (c) two
nanoparticles are arranged along the y direction with respect to the polarization directions of
pump and Stokes light fields being along the x direction.

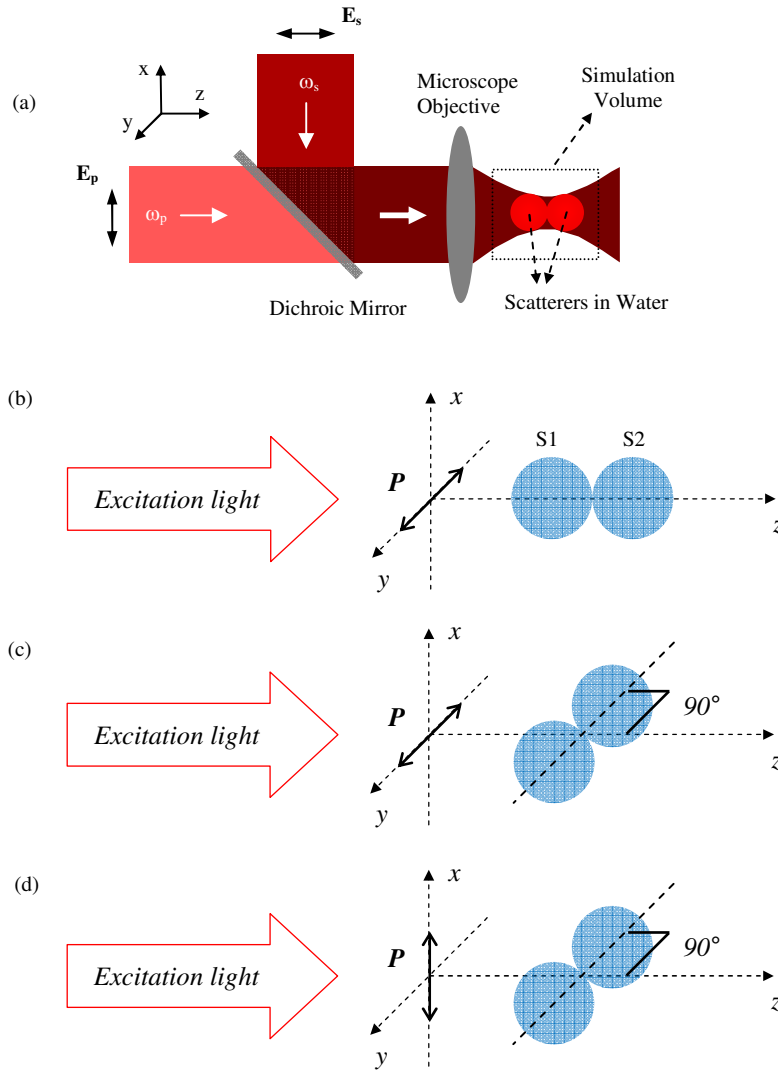


Fig. 1. Schematic diagram of CARS experiments (a) and three different configurations of nanoparticles' orientations with respect to the polarizations of the pump and Stokes light fields (b, c, d).

3. Results and discussion

3.1 Influence of scatterers' orientations on excitation fields and near-field CARS signals

Figs. 2(a, b) depict the electric field distributions of the pump light with y-polarization in the y-z plane for the two different nanoparticle orientations: (a) along the z-direction, and (b) along the y-direction. The corresponding amplitude profiles of E_y are displayed in Figs. 2(a) and 2(b), respectively. Similar field distribution for the Stokes light on the y-z plane of the nano-scatterers is also obtained (data not shown). The excitation light field is significantly enhanced at the scatterer-water interface especially in the y direction (red curves indicated in Figs. 2(c) and 2(d)). This phenomenon could be attributed to the near-field enhancements (e.g., the generation of the non-propagating evanescent waves due to the index mismatch at the nanoparticles/water interface [21, 26]. As the refractive index of nanoparticles is much larger

than the surrounding water, the conservation of the electric displacement D at the interface leads to an enhanced electric field in water [21, 31]. When the nanoparticles oriented along the z direction, the amplitude of the electric field inside the particles remains a relative constant (fluctuation $<10\%$, blue curve in Fig. 2(c)); however, when the scatterers are oriented along the y direction that is parallel to the excitation light polarization, the corresponding amplitude of the electric field between the scatterers is approximately 1.8-fold higher than that at the nanoparticle-water interface (Fig. 2(d)). This can be subjected to the enhancement effect of the constructive interference of the enhanced near-fields between the scatterers. Hence, the excitation field distributions due to different scatterers' orientations under different excitation polarizations can significantly affect the near-field CARS generations.

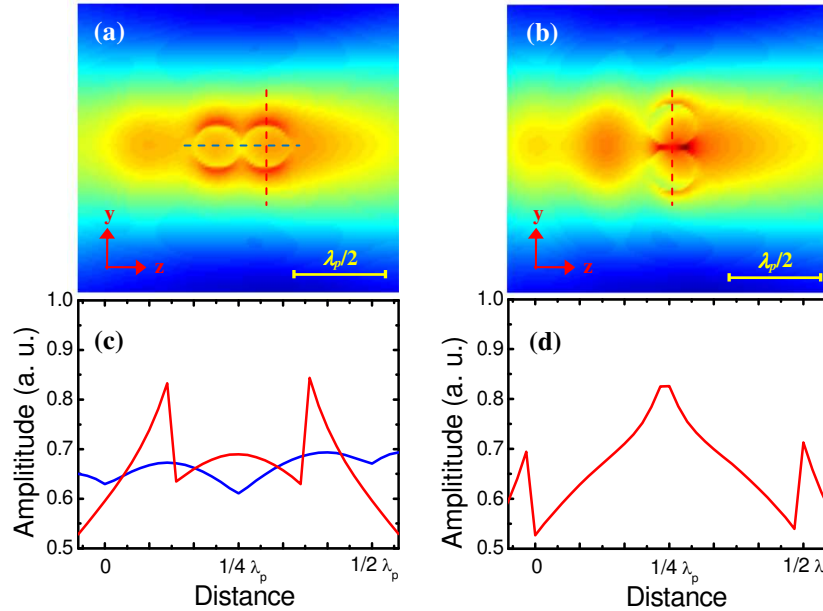


Fig. 2. Distributions of the focused pump field E_y with y -polarization in the y - z plane for the two scatterers arranged in the z -direction (a) and in the y -direction (b). (c) and (d) are the corresponding amplitude profiles along the dashed lines in 2(a) and 2(b), respectively.

Figures. 3(a, b) show the distributions of the induced third-order polarizations (P_y) in the y - z plane under the excitation polarizations in the y -direction and the scatterers' orientations along the z -direction and the y -direction, respectively, and the corresponding amplitude profiles are displayed in the bottom panel. When the nanoparticles arranged along the z direction (Fig. 3(a)), the induced CARS signals have a sharp peak at the vicinity of nanoparticle-water interface along the y direction due to the refractive index mismatch as elaborated above. The CARS amplitude inside the nanoparticles is approximately a quarter smaller than the peak signal at the nanoparticles/water interface. However, when the nanoparticles oriented along the y direction (Fig. 1(c)), the CARS peak signal at the upper and lower surfaces of nanoparticles decreases by 40% compared to the CARS signal from the particles arranged along the z -direction, and the CARS signal between the nanoparticles remarkably increases, yielding an approximately 2-fold improvement in intensity compared to the signal at the particle/water interface (second panel of Fig. 3(b)). Hence, the orientations of nanoparticles arranged parallel to the polarization direction of excitation light fields are more favorite for generating larger near-field CARS radiations.

Figures 3(c, d) show the induced nonlinear polarizations components (P_x) in the x - y plane which is perpendicular to the excitation polarization under the configurations shown in Figs.

1(b) and 1(c), respectively. Compared with the component P_y parallel to the excitation field polarization (Figs. 3(a, b)), the perpendicular component P_x is about one order of magnitude smaller than the component P_y (Figs. 3(c, d)). On the other hand, the P_x component of CARS signals is mainly confined within the subsurface of nanoparticles or at the nanoparticles/water interface. It can also be seen from the amplitude profiles in the second panel of Figs. 3(c, d) that the perpendicular component P_x has a very sharp peak with a full width at half maximum (FWHM) of $\sim \lambda_p/16$ which is at least 4 times narrower than the FWHM of P_y (Fig. 3(b)). Furthermore, the image contrast of CARS signals provided by the perpendicular component P_x can reach up to 200 (Fig. 3(c)). These superior features arising from the perpendicular component of near-field CARS imaging could be utilized for revealing the very fine structures of cells (e.g., membrane, mitochondria) with nanoscale resolutions (resolution of 47 nm (=750 nm/16)).

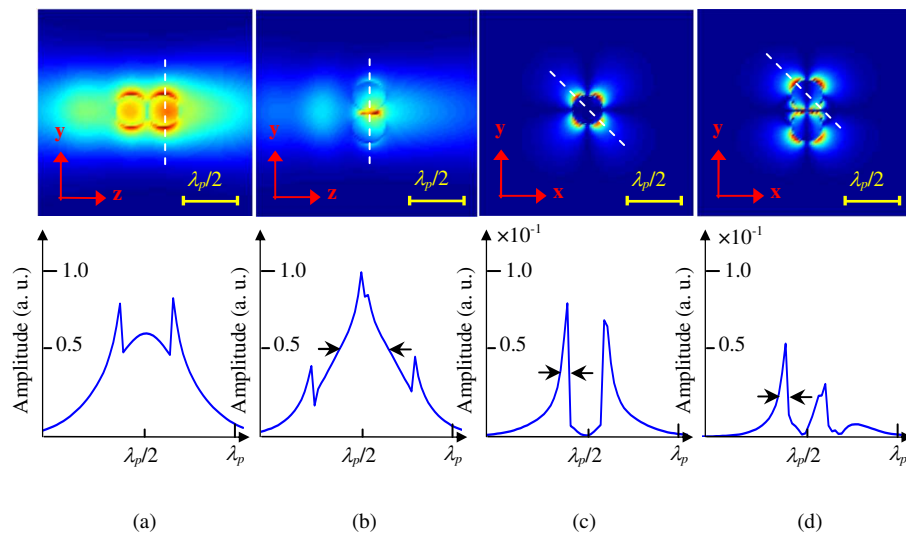


Fig. 3. Distributions of the induced third-order polarizations (P_y components) in the y - z plane under the excitation polarizations in the y -direction and the scatterers' orientations along the z -direction (a) and the y -direction (b). Distributions of the induced third-order polarizations (P_x components) in the x - y plane under the excitation polarizations in the y -direction and the scatterers' orientations along the z -direction (c) and the y -direction (d). The corresponding amplitude profiles along the dashed lines in the top panel are displayed in the bottom panel.

3.2 Influence of the excitation light polarization on near-field CARS signals

If the two nanoparticles are oriented along the z direction as shown in Fig. 1(b), they have rotational symmetry along the z -axis, such that the field distribution and also the generated CARS radiation pattern will not be affected by the change of polarization directions of the excitation light fields (no matter changing to the x - or y - direction). But this is not the case when the scatterers are arranged perpendicularly to the z -direction as shown in Figs. 1(c, d).

Figure 4 shows the distributions of the P_x component in the y - z plane, x - y plane and the P_y component in the x - y plane, respectively, under the excitation light polarization along the x -direction. The P_x intensity in the y - z plane inside the nanoparticles is about 2 times stronger than that in surrounding water, and there is an intensity drop due to destructive interference of CARS fields between the two nanoparticles (Fig. 4(a)). But the enhanced near-field CARS signals can be observed at the nanoparticle-water interface along the x direction, due to the refractive index mismatch at the interface (Fig. 4(b)). On the other hand, the induced polarization component P_y , which is perpendicular to the excitation light polarization also gives a strong near-field CARS signal within the subsurface of nanoparticles or at the

nanoparticles/water interface with a FWHM of $\sim \lambda_p/16$ (Fig. 4(c)) which is at least 4 times narrower than the FWHM of P_y (Fig. 4(b)). By comparing the near-field CARS results between the two different excitation configurations (Figs. 1(c, d)), the parallel component of the induced nonlinear polarization in Figs. 4(a, b) is about 80% lower than that in Fig. 3(b), and the perpendicular component in Fig. 4(c) is 55% lower than that in Fig. 3(d). It should be pointed out that the contrast of near-field CARS images for the perpendicular components under the two different excitation configuration (Figs. 1(c, d)) can give rise to 200 with a FWHM of $\lambda_p/16$ (Figs. 3(c) and 4(c)). This again confirms the possibility of applying the perpendicular near-field CARS component for high sensitive and high contrast molecular imaging in cells with nanoscale resolutions.

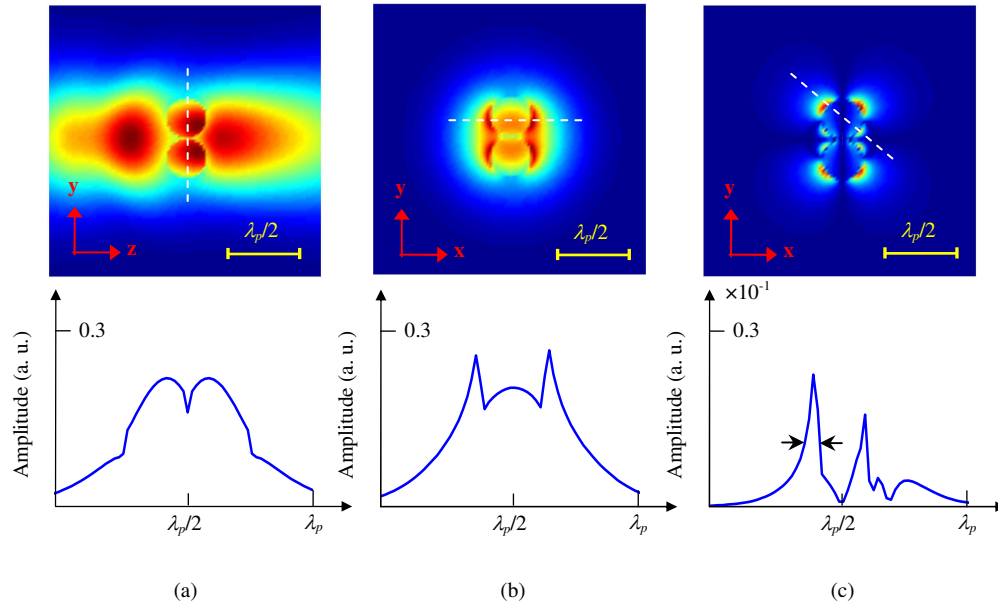


Fig. 4. Distributions of the induced polarization component P_x in the y - z plane (a); in the x - y plane (b); and the component P_y in the x - y plane (c), respectively. The bottom panel shows the corresponding amplitude profiles along the dashed lines indicated in the top panel. Note that the scatterers are oriented along the y -direction while the excitation light polarization is along the x -direction (Fig. 1(d)).

3.3 Effect of the scatterer's size on near-field CARS signals

Figures 5(a-e) show the induced nonlinear polarizations (P_y) in the y - z plane for nanoparticles with diameters of $\lambda_p/4$, $3\lambda_p/8$, $\lambda_p/2$, $3\lambda_p/4$, and λ_p , respectively, under the excitation light polarization along the y -direction. The first and the second panels show the amplitude distributions under the excitation configurations indicated in Figs. 1(b, c), respectively, and the corresponding amplitude profiles are displayed in the bottom panel. It is observed that when the nanoparticles are orientated along the z direction, the induced nonlinear polarizations inside nanoparticles increase up to 3.5-fold with the increased diameters of nanoparticles (ranging from $\lambda_p/4$ to λ_p) (red curves shown in the third panel of Fig. 5). This probably is due to the reason that with the increased scatterer's sizes, the incident excitation light tends to be more focused onto larger nanoparticles, leading to a stronger excitation light field distributions inside the larger nanoparticles than those in smaller nanoparticles. On the other hand, it is also found that the near-field enhancement at the nanoparticles/water interface decreases with the increased nanoparticle's sizes (data not shown). This phenomenon could be attributed to the weaker efficiency of generation of evanescent waves associated with larger nanoparticles [21]. In contrast, when the nanoparticles are orientated parallel to the excitation

light polarization (Fig. 1(c)), the amplitude of the induced nonlinear polarizations (P_y) decreases by almost 50% with the increased diameters of nanoparticles (ranging from $\lambda_p/4$ to λ_p) (black curves shown in the third panel of Fig. 5). One notes that if the diameters of nanoparticles are less than $3\lambda_p/8$, the induced nonlinear polarization (P_y) between the nanoparticles is about 1.7-fold larger for the particles orientated parallel to the excitation light polarization than that for the particles aligned perpendicularly to the excitation light polarization (shown in the third panel of Figs. 5(a, b)); while the converse is true for the nanoparticles larger than $\lambda_p/2$ (shown in the third panel of Figs. 5(c-e)). Therefore, the near-field CARS enhancement between the nanoparticles is more dominant for smaller nanoparticles, while a more effective focusing of the excitation light fields can be observed from larger nanoparticles for generating near-field CARS radiations.

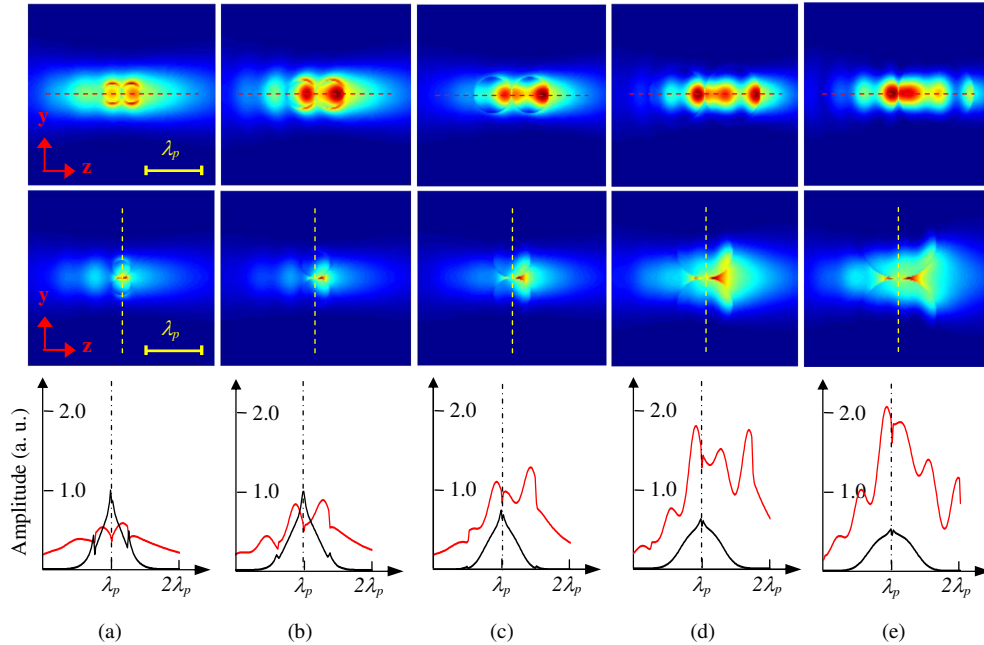


Fig. 5. The induced third-order nonlinear polarizations (P_y) in the y - z plane for nanoparticles with different diameters (a= $\lambda_p/4$; b= $3\lambda_p/8$; c= $\lambda_p/2$; d= $3\lambda_p/4$; e= λ_p) under the excitation light polarization along the y -direction with the nanoparticles orientated in the z -direction (first panel), and the y -direction (second panel), respectively. The corresponding amplitude profiles along the dashed lines in the first and second panels are displayed in the bottom panel.

We also study the change of the induced nonlinear polarization component (P_x) of the nanoparticles in the x - y plane which is perpendicular to the y -polarized excitation light with respect to different diameters of nanoparticles ((a)= $\lambda_p/4$, (b)= $3\lambda_p/8$, (c)= $\lambda_p/2$, (d)= $3\lambda_p/4$, (e)= λ_p) (Fig. 6). The first and the second panels show the amplitude distributions under the excitation configurations indicated in Figs. 1(b, c), respectively. The corresponding amplitude profiles along the dashed lines in the first and second panels are displayed in the bottom panel. The perpendicular components of the induced polarization (P_y) decrease with the increased nanoparticle's diameters (ranging from $\lambda_p/4$ to λ_p) for the two different nanoparticles' orientations (Figs. 1(b,c)); while the near-field CARS peak positions gradually shift from the nanoparticle/water interface into the inner side of nanoparticles with the FWHM increasing rapidly from less than $\lambda_p/16$ (Fig. 6(a)) up to over $\lambda_p/4$ (Fig. 6(e)). Obviously, the near-field CARS enhancement at the nanoparticles/water interface becomes more dominant for smaller nanoparticles ($\leq \lambda_p/2$) (Figs. 6 (a-c)). This can also be related to the effective generation of evanescent waves associated with smaller nanoparticles [21, 23]. The above results reconfirm

that no matter the small scatterers ($\leq \lambda_p/2$) are orientated parallel or perpendicularly to the light propagation direction, the perpendicular polarization component of the induced near-field CARS radiations is always strictly confined within the subsurface of scatterers or the scatterer/water interface, leading to high sensitive and high contrast molecular imaging with high spatial resolutions (down to $\lambda_p/16$).

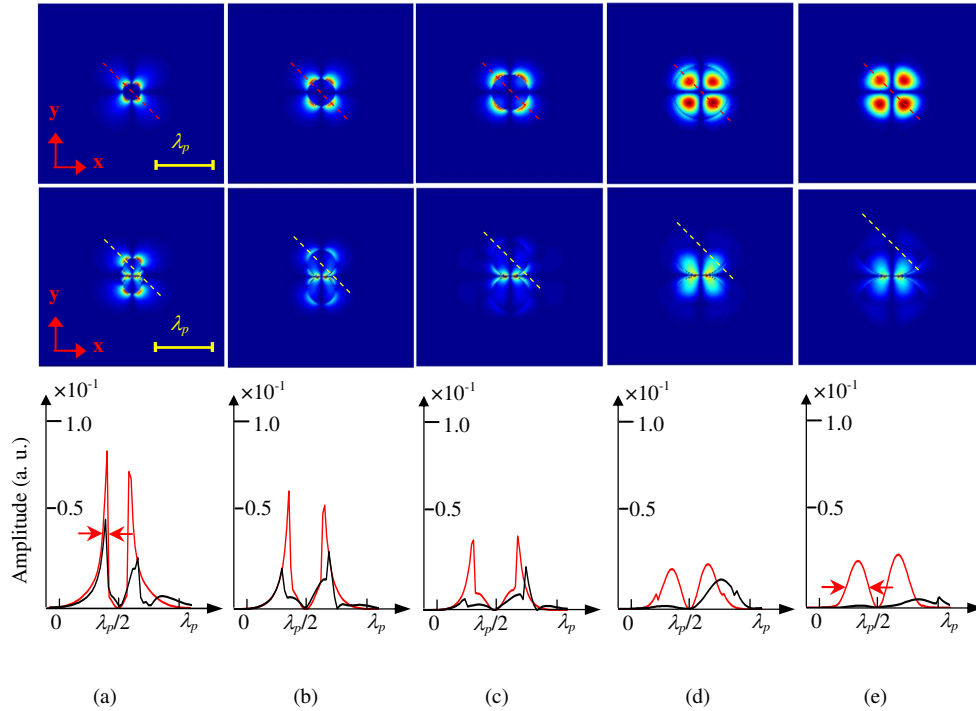


Fig. 6. The induced nonlinear polarizations (P_x) in the x-y plane under the excitation light polarization along the y-direction for nanoparticles with different diameters ($a = \lambda_p/4$; $b = 3\lambda_p/8$; $c = \lambda_p/2$; $d = 3\lambda_p/4$; $e = \lambda_p$) being orientated in the z-direction (first panel), and the y-direction (second panel), respectively. The corresponding amplitude profiles along the dashed lines in the first and second panels are displayed in the bottom panel.

In this work, we applied the advanced numerical technique based on the finite-difference time-domain (FDTD) method to numerically resolve Maxwell's equations without the need of boundary conditions for studying the influences of the excitation light polarization, the scatterers' sizes and orientations in water on the near-field CARS signal generations. The simulation results show that the near-field CARS radiations strongly depend on the excitation light polarization, the nanoparticles' sizes and orientations (Figs. 2-6). For the scatterers with physical sizes of much less than the excitation light wavelength, the excitation light fields can be strongly enhanced owing to the generations of evanescent waves particularly at the scatterer-water interface, as well as the light field interference between the nanoscatterers, resulting in an additional highly localized excitation light field (Fig. 2) for enhancing near-field CARS radiations (Figs. 3-6). Compared to the near-field light field distributions and CARS radiations generate from a single nanoscatterer configuration [26], the local field enhancements from the two nanoscatterers owing to the near-field effect (e.g., evanescent wave generation) and also light field constructive interference between the two nanoscatterers can be significantly improved. For instance, the local field enhancement for the scatters with diameters of $\sim \lambda_p/4$ can be 2.2 times stronger, resulting in a 4.5-fold improvement in the near-field CARS signals compared to the single nanoscatter configuration [26]. Our further simulations show that the enhancement of the perpendicular component of near-field CARS

signals only takes place in the regions within the scatterer-water interface or the subsurface of the scatterers, leading to a high sensitive and high contrast molecular imaging with a spatial resolution of down to $\lambda_p/16$ that is far beyond the diffraction limit of optics system [32]. Therefore, near-field effects can play a significant role in nanoscale CARS microscopy. With the advantages of the perpendicular polarization which is strictly confined to the scatter-water interface, the perpendicular polarization near-field CARS microscopy can be potentially useful to provide high contrast of CARS images for revealing very fine structures of inter- and/or intra- cellular organelles (e.g., membrane) in cells with nanoscale resolutions. One notes that such near-field distributions and near-field CARS imaging could be directly mapped out by using near-field detection schemes, such as near-field scanning optical microscopy (NSOM) [20-23], and nonlinear optics (e.g., tip-enhanced CARS microscopy) [17-19], which can realize vibrational imaging of nanostructures far beyond the spatial resolution of far-field CARS microscopy.

Acknowledgments

This work was supported by the Academic Research Fund from the Ministry of Education, the Biomedical Research Council, the National Medical Research Council, and the Faculty Research Fund from the National University of Singapore.